A NODAL JACOBIAN INVERSE SOLVER FOR REDUCED COMPLEXITY EIT RECONSTRUCTIONS

B M GRAHAM AND A ADLER

Abstract. Electrical impedance tomography (EIT) uses surface electrodes to make measurements from which an image of the conductivity distribution within some medium is calculated. Calculation of conductivity solutions requires inverting large linear systems that have to date restricted reconstructions to 2D or coarse 3D domains. This paper presents a Nodal Jacobian Inverse Solver that scales with the number of nodes in a finite element mesh rather than with the number of elements. For the example used in this paper the size of the linear system is reduced by a factor of 26. We validate the algorithm by comparing its performance to traditional 2D Elemental Jacobian algorithms. We then analyze its performance with a 21504 element 3D mesh that is too large to be solved with linear algebra systems based on 32 bit pointers (such as is available in current versions of Matlab). Finally, we demonstrate the applicability of the algorithm for clinical use by reconstructing experimentally measured human lung data.

1. Introduction

Electrical Impedance Tomography (EIT) uses body surface electrodes to make measurements from which an image of the conductivity distribution within some medium is calculated. Calculation of conductivity solutions using one of the Newton type methods requires inverting large linear systems derived from finite element models of the medium under analysis. The Hessian matrix in these linear systems scale with the square of number of elements in the model and the square of the number of measurements used in the reconstruction. Almost all EIT algorithms use a piecewise constant conductivity model, in which the conductivity is considered to be constant over an element. The large number of elements required and large number of measurements available for 3D reconstructions have to date restricted 3D reconstructions to coarse, low resolution models. Complex, accurate geometries, *a priori* structures, the increased number of measurements possible with newer machines and the desire for improved resolution in the third dimension leads to a requirement to solve large 3D models. Such reconstructions are beyond the capability of contemporary computers such as the AMD Athlon 64 3000+, 2GB RAM computers used in our lab. Thus the development of algorithms that can efficiently calculate full 3D solutions over dense finite element models with many measurements is required.

In this paper we present and evaluate a *Nodal Jacobian Inverse Solver* algorithm that reduces the execution time and memory required to calculate reconstructions. In addition to gains in reconstruction efficiency, the extraction and display of data stored in the nodal format is much quicker than for data stored in the elemental

format. Moreover, nodal solutions are easily processed using pixel based filtering algorithms similar to those used in image processing work.

The finite element model used in this work includes a mesh that has a simple cylindrical geometry but is comprised of over 20,000 elements. This high mesh density is not warranted for a 16 electrode-208 measurement protocol, however it is used in this work to show the performance improvement possible using the proposed solver. It is expected that applications that use many electrodes or require huge numbers of elements to model complex geometries will be able exploit the performance benefits of the proposed algorithm.

2. Methods

This paper introduces the *Nodal Jacobian Inverse Solver* as follows. In the methods section we describe the traditional family of EIT reconstruction algorithms used in our research, describe the *Nodal Jacobian* variation of this family of algorithms, and describe the evaluation procedure. In the results we describe the effectiveness of the new family of algorithms compared to the traditional algorithms. In the discussion we consider some additional observations of this work and conclude with a recommendation of the proposed algorithm.

2.1. Data Acquisition. Lab data used in this paper was obtained using a 16 electrode adjacent drive EIT machine (the Goe-MF II type tomography system, Viasys Healthcare, Höchberg, Germany) designed for use with 2D reconstruction algorithms based on data from electrodes placed in a planar section of the medium as shown in figure 1(a). Adjacent current stimulation is used with adjacent voltage measurement at all remaining electrodes except the driven electrode pair. The general formula for the number of measurements obtained using this type of injection-measurement protocol is $M = (N_{el} - 3)/N_{el}$ where N_{el} is the number of electrodes. For 16 electrodes, 208 measurements are available per frame, while for a 32 electrode system the number of available measurements is 928. Although the 16 injection-measurement patterns are obtained over a finite time interval, 80ms for the Goe-MF II, the entire vector of 208 measurements is treated as representing the boundary voltages at a single instant in time and is considered a *frame* of data.

Data obtained from a 2D electrode placement such as in figure (1(a)) is most often used to calculate a 2D estimate of the conductivity although a 3D reconstruction algorithm could use these data. By placing the electrodes in multiple planes 2D equipment can be used to acquire data that are better suited for 3D reconstructions. One such method is the hybrid electrode placement strategy [8] shown in figure 1(b) in which electrodes are placed in two axially aligned planes with the 16 electrodes connected sequentially as shown by the numbers in the figure. This arrangement will result in an inter-plane injection-measurements between electrodes 8 and 9 as well as 16 and 1. This strategy is used in this work in order to validate some of the simulated results with lab data collected using the Goe-MF II. The EIDORS v3 suite [2], using the Complete Electrode Model, was extended to perform the work in this paper.

2.2. EIT Modeling. We consider EIT difference imaging, which is widely understood to improve reconstructed image stability in the presence of problems such as unknown contact impedance, inaccurate electrode positions, non linearity, and the use of 2D approximations for 3D electrical fields when reconstructing in 2D [3] [10]. We address the class of one-step linearized reconstruction algorithms that calculate the change in a finite element conductivity distribution $\mathbf{x} = \sigma_2 - \sigma_1$ due to a change

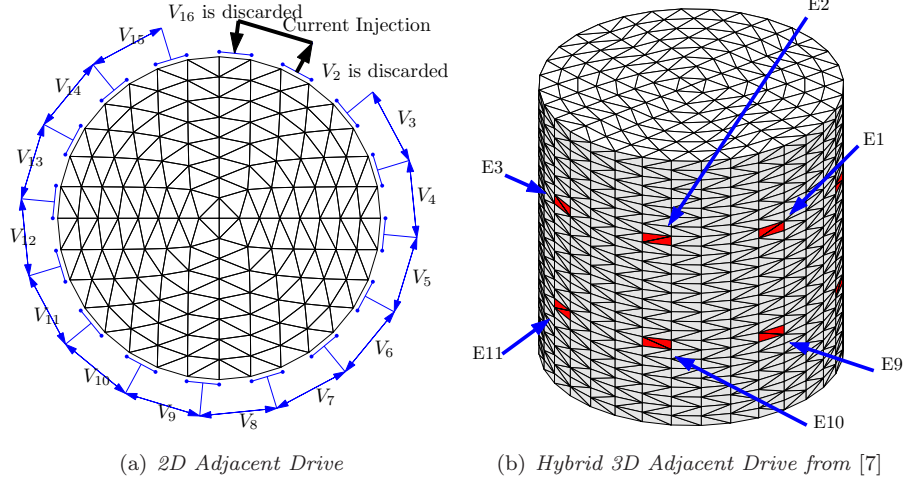(a) *2D Adjacent Drive*

(b) *Hybrid 3D Adjacent Drive from* [7]

FIGURE 1. *Data Acquisition Setup. 28 Layer Reconstruction Mesh, 21504 Elements, 4205 Nodes. Electrodes are arranged in two layers of 8 electrodes.*

in difference signal, $\mathbf{z} = \mathbf{v_2} - \mathbf{v_1}$, over a time interval (t_1, t_2). By convention we consider the signal at t_1 to be the *reference* frame and the signal at t_2 to be the *data* frame. Since we do not know σ_1, $\mathbf{x}$ is interpreted as the change in conductivity with respect to the unknown initial conductivity $\mathbf{x} = \mathbf{\Delta}\sigma$.

A forward model is required when one wants to solve the non-linear problem, generate simulated data or calculate the Jacobian using the efficient method described in [13] that requires calculation of the electric fields in the interior of the object. Using the finite element method (FEM), the voltage distribution at E electrodes is simulated by current injection into the medium with a conductivity distribution discretized on N finite elements. This model of the forward problem accepts a vector of conductivity values and calculates the voltage V_{ij} at each node i for each current injection pattern j through the linear equation

$$(1) \qquad \mathbf{V} = \mathbf{Y}(\sigma)^{-1}\mathbf{I}$$

where $\mathbf{Y}(\sigma)$ is the admittance matrix of the FEM and I_{ij} is the current at each node i during current injection pattern j. With the point electrode model each electrode is modeled as a single boundary node, thus the columns of I have only two non-zero entries corresponding to the current injected at the two electrodes. Calculation of the vector $\mathbf{v}$ of M voltage differences is represented by $\mathbf{v} = T[\mathbf{V}(\sigma)]$. For instance if v_9 is defined to correspond to the voltage difference between electrodes 4 and 5 during injection pattern 2, then the operator T will give $T[\boldsymbol{V}]_9 = \boldsymbol{V}_{42} - \boldsymbol{V}_{52}$.

The most accurate mathematical model for EIT is the complete electrode model (CEM)

$$(2) \qquad \begin{bmatrix} A_M + A_Z & A_W \\ A_W^T & A_M \end{bmatrix} \begin{bmatrix} \Phi \\ V \end{bmatrix} = \begin{bmatrix} 0 \\ I \end{bmatrix}$$

where A_M, A_W, and A_Z represent the CEM boundary conditions. In this paper we use the point electrode model for the 2D experiments and the CEM for the 3D experiments. A complete derivation of the CEM can be found in [14] however the salient point is that in (1) and (2) $A_M = Y$ is the N by N symmetric admittance

matrix given by

$$(3) \qquad Y_{ij} = \int_{\Omega} \sigma \nabla w_i \cdot \nabla w_j d\Omega$$

where w_i is a linear basis function with value 1 on i^{th} node and 0 elsewhere. In the usual case σ is considered constant on each element (piecewise constant) which allows σ to be brought outside the integral in (3)

$$(4) \qquad Y_{ij} = \sum_{k=1}^{N} \sigma_k \int_{\Omega_k} \nabla w_i \cdot \nabla w_j d\Omega_k$$

The integral in (4) is calculated analytically for each element with each element contributing 9 (for a triangle) or 16 (for a tetrahedron) entries to the master admittance matrix Y.

For small changes around a background conductivity the relationship between $\mathbf{x}$ and $\mathbf{z}$ may be linearized as

$$(5) \qquad \mathbf{z} = \mathbf{Hx} + \mathbf{n}$$

where $\mathbf{H}$ is the Jacobian or sensitivity matrix and $\mathbf{n}$ is the measurement system noise, assumed to be uncorrelated additive white Gaussian (AWGN).

For piecewise constant conductivity models, each element i, j, of $\mathbf{H}$ is defined as $H_{ij} = \left. \frac{\partial z_i}{\partial x_j} \right|_{\sigma_0}$ and relates a small change in the ith difference measurement to a small change in the conductivity of jth element with respect to a background conductivity vector, σ_0. $\mathbf{H}$ is a function of the FEM, the current injection pattern, the measurement pattern, and the background conductivity. We use the adjacent current injection pattern and a homogenous background conductivity with $\sigma_0 = 1$ for each of the elements. $\mathbf{H}$ is a matrix comprised of E columns of length M where E is the number of elements in the finite element model and M is the number of measurements per frame. Thus the ith column represents the change in the M boundary measurements due to a change in the conductivity of the ith element. There are several ways to calculate the Jacobian; the EIDORS2D toolset [15] uses the *Standard Method* [14][18] whereas the EIDORS3D toolset [12] uses a more efficient method involving the dot products of the interior electric fields.

2.3. Image Reconstruction. In order to overcome the ill-conditioning of $\mathbf{H}$ we solve (5) using the following regularized inverse originally described in [1]

$$(6) \qquad \hat{\mathbf{x}} = (\mathbf{H}^T \mathbf{W} \mathbf{H} + \lambda^2 \mathbf{R})^{-1} \mathbf{H}^T \mathbf{W} \mathbf{z} = \mathbf{Bz}$$

where $\hat{\mathbf{x}}$ is an estimate of the true change in conductivity, $\mathbf{R}$ is a regularization matrix, λ is a scalar hyper parameter that controls the amount of regularization, and $\mathbf{W}$ models the system noise. We calculate λ using the *BestRes* algorithm described in [7]. Noise is modeled as uncorrelated with conductivity changes and among measurement channels; thus, $\mathbf{W}$ is a diagonal matrix with $W_{i,i} = 1/\sigma_i^2$ where σ_i^2 is the noise variance for measurement i. $\mathbf{W}$ can also be modified to account for variable gain settings on each tomograph channel. With $\mathbf{R} = \mathbf{I}$ (labeled $\mathbf{R}_{Tik}$) equation (6) is the 0th order Tikhonov algorithm. With $\mathbf{R} = diag(\mathbf{H}^T\mathbf{H})$ (labeled $\mathbf{R}_{diag}$) equation (6) is the regularization matrix used in the NOSER algorithm [5]. In [1] $\mathbf{R}$ is a model of the inverse *a priori* image covariance. EIT has the potential for only a relatively few independent measurements. As a direct consequence there will be limited high spatial frequency content, or low spatial resolution, associated with any reconstructed image. This implies that the elements with a separation less

than the minimum recoverable spatial period (EIT resolution) are highly correlated. Consequently Adler and Guardo [1] model $\mathbf{R}$ as a spatially invariant Gaussian high pass filter (labeled $\mathbf{R}_{HPF}$) with a cut-off frequency selected so the spatial period is a given fraction of the medium diameter. In two dimensions a Gaussian high pass filter of spatial frequency ω_0 has the form

$$(7) \qquad \mathbf{F}(u, v) = 1 - e^{-\omega_0(u^2 + v^2)}$$

In the spatial domain the convolution kernel is

$$(8) \qquad f(x, y) = \delta(x, y) - \frac{\pi}{\omega_0^2} e^{-\left(\pi^2/\omega_0^2\right)\left(x^2 + y^2\right)}$$

where $\delta(x, y)$ is the Dirac delta function. The filtering matrix $\mathbf{F}$ multiplies an image vector $\mathbf{x}$ to give a filtered image $\mathbf{Fx}$. F_{ij} is calculated by centering the high pass filter in element i and integrating across element j

$$(9) \qquad F_{ij} = \int_{E_j} \left[\delta\left(x - x_i, y - y_i\right) - \frac{\pi}{\omega_0^2} e^{-\left(\pi^2/\omega_0^2\right)\left((x - x_i)^2 + (y - y_i)^2\right)} \right] dx dy$$

This integration is performed numerically on a mesh of 512×512 points superimposed over the 2D FEM. We define this as an integration density of 512 points per linear unit or 512^2 points per square unit. The filter cut-off frequency is expressed in terms of the percentage of the diameter. Using a mesh of N_p points

$$(10) \qquad (\% \text{ diameter}) = \frac{N_p}{2\pi\omega_0}$$

The regularization matrix is calculated as $\mathbf{R}_{HPF} = \mathbf{F}^T\mathbf{F}$. This filter could be extended to 3D by including the z component in equation (9) and integrating numerically over a mesh of integration density 512^3 points per cubic unit; however we do not use a 3D version of the Gaussian filter in this paper.

Although all three of these priors are smoothing filters which attenuate the contribution of the high frequency components of the SVD of $\mathbf{H}^T\mathbf{H}$, the Gaussian high pass filter has the advantage of being mesh size and mesh shape independent in that it is a function of the area weighted mesh inter-element correlations.

2.4. Nodal Jacobian. As the number of elements in a FEM increases, the time and memory required to calculate the solution increases, such that solving problems of useful resolution in 3D becomes difficult or impossible to perform. For example the term $\mathbf{H}^T\mathbf{WH}$, in equation (6) for the 21504 element FEM of figure 1(b)) produces a matrix of size 21504×21504 which exceeds the memory capabilities of 32-bit matrix indexing arithmetic, such as is currently available in Matlab software.

The ratio of nodes to elements can be up to a factor of two for 2D FEM meshes; the sum of angles in a triangle is 180, a point has 360 degrees, thus a dense mesh will tend to have an element to node ratio of two. In 3D a point has a solid angle of 4π, six tetrahedra fit into a cube (solid angle of 4π); a tetrahedron therefore has solid angle of $4\pi/6$. Thus a dense mesh will tend to have an element to node ratio of six although practical meshes will have a lower ratio; the 3D mesh used in this paper has an element to node ratio of 5.1. The incentive to develop an algorithm that scales with the number of nodes rather than the number of elements is the fact that the size of the Hessian matrix will be reduced by the square of the element to node ratio. Thus the Hessian matrix for the 3D mesh used in this paper will be reduced by a factor of 26 which is sufficient to allow it to be formed within the 32-bit matrix indexing environment of Matlab.

The construction of a *Nodal Jacobian* is based on the development of a nodal finite element model. In [9] Kaipo *et al* introduce a 2D finite element model based on a piecewise linear discretization of the conductivity in which the conductivity of an element is linearly interpolated throughout its volume based on the conductivity values at its vertices. The adoption of piecewise linear conductivity on each element means that the conductivity cannot be brought outside the integral in equation (3) thus equation (4) cannot be used to calculate the admittance matrix rather we must solve

$$(11) \qquad\qquad Y_{ij} = \sum_{k=1}^{N} \int_{\Omega_k} \sigma_k(\vec{r}) \nabla w_i \cdot \nabla w_j d\Omega_k$$

where $\vec{r}$ is a position vector within element k. For an inhomogenous isotropic material $\sigma_k(\tilde{r})$ is a conductivity tensor of the form $\sigma_k(\tilde{r}) = \sigma_k(\tilde{r})I$ where $\tilde{r}$ is a scalar function of the conductivity and I is the identity matrix.

In [9] Kaipo *et al* use the same linear basis functions, w_i, for σ as are used for the potential. In [9] the authors do not discuss or exploit the complexity improvement associated with using the nodal basis. Their use of piecewise linear conductivity was motivated by a requirement to calculate the gradient of the conductivity within each element for the purposes of incorporating a structural prior into their reconstructions. By using a piecewise linear conductivity model the gradient over each element is a constant. An implementation of the piecewise linear element is available in the EIDORS2D toolset [15] in which Y is calculated from equation (11). Also provided is a function to calculate the corresponding Nodal Jacobian using the *Standard Method*.

EIDORS3D [12] calculates an Elemental Jacobian using the NSHI (nullspace scaled hybrid isotropic) algorithm described in [16]. The NSHI algorithm is over **60** times faster than the *Standard Method* for the example cited in [13] but requires components calculated from an element based master matrix. Thus in order to retain the speed advantage of the NSHI algorithm, we adapted the EIDORS2D nodal master matrix construction algorithm to construct a Nodal Jacobian, H^N, from the elemental Jacobian, H^E, as follows:

  1    $d = 3$ for triangles, $d = 4$ for tetrahedrons
  2   for each node, n, in the mesh
  3   elems=list of elements using node n
  4      $H^N_{:,n} = \sum_{i \in \text{elems}} 1/d H^E_{:,i}$ where $H_{:,i}$ means the ith column of matrix H
  5   end for each node

Intuitively this can thought of as having each element contribute an equal proportion of its sensitivity to each of its three or four contained vertices.

When using the *Nodal Jacobian* in the regularized inverse (6) the resulting solution will be in the nodal basis. It is possible to convert the nodal solution back to a piecewise constant element basis where it is determined by E parameters. Conversion back to an elemental basis can be done by setting the conductivity value for each element to an average of the conductivity values of its enclosing vertices. This has the advantage of being simple to implement and works well for meshes constructed of regularly spaced nodes. It is also possible to weigh the average as a function of subtended angle or Voronoi cell area. In either case the conversion to an elemental solution will introduce additional smoothing through local averaging which may or may not be desirable. In this paper we maintain solutions in the nodal basis.

Two advantages of the nodal basis are the ability to store the solution in a smaller number of parameters, and the ability to rapidly extract and render graphical displays of solutions using a function such as Matlab's built-in *trisurf* function. The *trisurf* function takes as input a list of vertices and associated values at each vertex. No explicit knowledge of the geometry is required, such as an element list providing connectedness between nodes, in order to display cut planes of coplanar nodes. For example the 3D model of figure (1(a)) has coplanar nodes at each of its 29 nodal layers as well as coplanar nodes at vertical slices such as $x = 0$ and $y = 0$ and other angles. Figure (7(a)) shows three multiplane conductivity representations of (1(a)) that were rendered by *trisurf* in real time (60ms each).

2.5. Nodal Gaussian Filter. The Gaussian High Pass filter, $\mathbf{R}_{HPF}$, of [1] can be extended to work over the nodes of the mesh as opposed to the elements. The regularization matrix is $\mathbf{R}_{HPF} = \mathbf{F}^T\mathbf{F}$ where F_{ij} is calculated by centering the high pass filter at node i and integrating across the Voronoi cell of node j in accordance with eq (9). As with equation (9) the filter cut-off frequency is expressed in terms of the percentage of the diameter in accordance with equation (10). This filter is extended to 3D by including the z component in equation (9) and integrating over the Voronoi polyhedra of node j. A Voronoi cell is polygon (polyhedra in 3D) whose interior consists of all points in the plane (hyper plane in 3D) which are closer to a particular node than to any other. Figure 2(b) shows part of a Voronoi diagram for a 64 element, 41 node FEM of figure 2(a). Note that there are no closed Voronoi cells for the nodes located on the boundary since they are by definition unbounded and extend to infinity. To overcome this problem for the 2D mesh, we add a set of auxiliary nodes by replicating the boundary nodes but located radially offset from the original location by a small distance (0.00001 was used for a mesh of diameter 1). Figure 2(c) is for illustrative purposes and shows the auxiliary nodes at an exaggerated stand off distance resulting in additional closed Voronoi cells. Figure 2(d) shows the auxiliary nodes located almost coincident with the boundary nodes which brings the outer Voronoi cell edge close to the boundary of the original mesh. The Voronoi cells, including the cells added through the auxiliary nodes, are used as the domain of integration for the Gaussian filter calculations. Note that it would also be possible to integrate each element in $\mathbf{F}$ over the basis function of each FEM node.
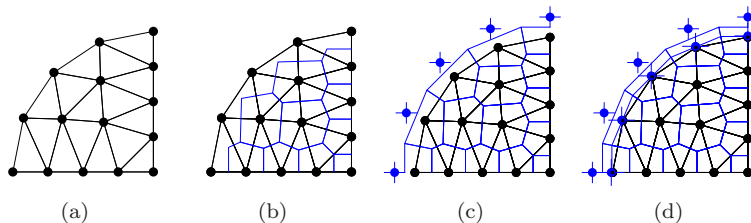

(a)   (b)   (c)   (d)

FIGURE 2. *One quarter of a 2D FEM showing development of Voronoi Cells for boundary nodes.*

The 3D models used in this work are constructed by using layers of nodes that are replicated and shifted versions of the nodes of an initial 2D mesh. The 3D Voronoi cell for such a mesh is an extruded version of the 2D Voronoi cell. This permits the numerical integration of the 3D Gaussian filter using equation (9). We

use equation (9) and integrate with an integration density of 512^3 points per cubic unit.

2.6. Laplacian Mask Filter. A further advantage of a nodal basis is that it facilitates the use of filters derived from pixel oriented domains such as found in the image processing literature. Rather than develop a low pass filter and then invert it, we follow the method of [1] and develop a high pass filter directly (based on the Laplacian mask described in [6] labeled $\mathbf{R}_{Lap}$ that is subsequently inverted in equation (6). We define the region of support for the Laplacian as nodes located with in a radius of some percentage of medium diameter. In this work we use 10%, a number arrived at through experience. The filtered value for node i is calculated as follows

$$\text{(12)} \qquad \hat{x}'(i) = (1 - \hat{x}(i)) \sum_{n \in \Omega_i} \hat{x}(n)(r/d_n)$$

where $\hat{x}(i)$ is the prior value of node i, r is the radius of the neighborhood, d is distance between node i and node n. Ω_i represents the radial neighborhood of node i; members of the set Ω are nodes that are located within a distance r of node i. $n \in \Omega_i$ means that n belongs to the radial neighborhood of node i. r/d_n is a weighing of the nodal value. This formulation for a Laplacian filter is mesh size independent which is different from the discrete Laplacian filters used in [12] and [4].

2.7. Smoothing Mask Filter. In addition to the filters used directly in the regularized inverse it is also possible to apply a spatial smoothing filter, $\mathbf{R}_{LP}$, to the nodal solutions of equation (6) by multiplying the solution with the low pass filter. This can be treated as a post processing step that increases the signal-to-noise ratio (SNR) of the solution. This filter is implemented through matrix multiplication as $\hat{\mathbf{x}}' = \mathbf{R}_{LP}^k \hat{\mathbf{x}}$. The exponent k indicates that this filter can be applied multiple times. In this paper we use $k = 1$ but other values are possible. $\mathbf{R}_{LP}$ calculates a filtered value for node i as follows

$$\text{(13)} \qquad \hat{x}'(i) = \sum_{n \in \Omega_i} \hat{x}(n)/\|\Omega_i\|$$

where $n \in \Omega_i$ means that n is a member of the radial neighborhood of node i including node i and $\|\Omega_i\|$ means the number of members of Ω_i. We incorporate $\mathbf{R}_{LP}$ into equation (6) before hyperparameter selection. Thus equation (6) with $\mathbf{W} = \mathbf{I}$ is restated as

$$\text{(14)} \qquad \hat{\mathbf{x}} = \mathbf{R}_{LP}^k (\mathbf{H}^T\mathbf{H} + \lambda^2\mathbf{R})^{-1}\mathbf{H}^T\mathbf{z}$$

with hyperparameter selected using the *BestRes* algorithm described in [7]. The complete algorithm can then be performed with any $\mathbf{z}$

2.8. Evaluation Procedure. In order to evaluate the performance of this algorithm, the following test procedures were conducted.

(1) Initially we validate the performance of the new algorithm by comparing its performance to the traditional algorithm for 2D reconstructions using tank data of an impulse phantom. Comparisons are made between the nodal and elemental Jacobians using the $\mathbf{R}_{Tik}$, $\mathbf{R}_{diag}$, $\mathbf{R}_{HPF}$ and $\mathbf{R}_{Lap}$ priors.
(2) We validate the 2D hyperparameter selection method, *BestRes*, [7] for 3D reconstructions.

(3) We quantify the performance of the 3D nodal algorithm using the $\mathbf{R}_{Tik}$, $\mathbf{R}_{diag}$, $\mathbf{R}_{HPF}$ and $\mathbf{R}_{Lap}$ priors, with two sets of simulated impulse phantom data. Both sets of simulated data were created by moving an impulse contrast through 28 vertical positions of a 28 layer, 86016 element, 15805 node FEM that is similar to, but denser than the FEM of figure 1(b). Reconstructions are made using the 21504 element mesh of figure (1(b)) One set of data had the impulse contrasts located at the axial center ($r = 0$), the second set of data had the contrasts located halfway between the axial center and the tank boundary ($r/2$).

(4) Finally we validate the *Nodal Jacobian* algorithm with some lab data of human lungs.

Quantitative figures of merit are required in order to compare the accuracy of the reconstructed images. Several figures of merit for EIT proposed in the literature were reviewed in [17]. The primary figures of merit used in this work are resolution, image energy, and signal to noise ratio of the reconstruction. We define *resolution* in terms of blur radius (BR). BR calculates the area fraction of the elements that contain the largest amplitude contributions to 50% of the total image amplitude and is therefore a measure of the concentration of image amplitude. BR is defined as $BR = r_z/r_0 = \sqrt[3]{V_z/V_0}$ for 3D, where r_0 and V_0 are the radius and volume respectively of the entire medium and r_z and V_z are the radius and volume of the reconstructed contrast containing half the magnitude of the reconstructed image [1]. In 2D, V represents area and a square root is taken. Image Energy, a global measure, is defined as $P = \sum_i \hat{x}_i^2 V_i$. For elemental solutions $\hat{x}_i$ is the solution amplitude at element i, while for nodal solutions $\hat{x}_i$ is the solution amplitude at node i. Signal to Noise Ratio is defined as $SNR = \overline{\hat{x}V}/\sigma_{\hat{x}V}$ which is the volume weighted, solution mean over the volume weighted, solution standard deviation). Again area is used for 2D. For elemental solutions the area and volumes used are those of the element triangles (2D) and tetrahedrons (3D), for nodal solutions the Voronoi cell area is used in 2D while the extruded Voronoi cell is used for 3D.

3. Results

3.1. 2D Results. We initially validated the performance of the nodal algorithm by calculating 2D reconstructions using data collected from a single plane of electrodes arranged around the middle of a tank. This is 3D tank data reconstructed with the assumption that the fields are confined in 2D. The phantom data used are from a 2cm non-conductive sphere located at r/2 in a tank of diameter 29cm and height 29cm. Data were collected using the Goe-MF II using the adjacent protocol described in section (2.1). Figure 3 shows reconstructions made using the $\mathbf{R}_{Tik}$, $\mathbf{R}_{diag}$, and $\mathbf{R}_{HPF}$ priors with the element based Jacobian. Figure 4 shows the same data reconstructed over the same mesh using the nodal based Jacobian and the $\mathbf{R}_{Tik}$, $\mathbf{R}_{diag}$, $\mathbf{R}_{HPF}$ and $\mathbf{R}_{Lap}$ priors. Resolution and signal to noise ratio are indicated in the figures.

Figures 3 and 4 show reconstructions normalized so that the vertical axis and color scales are maximized. The nodal algorithms produce much larger peak signals than the corresponding elemental solutions; however, this can be compensated for through normalization which is how the solutions of figures 3 and 4 are displayed. Resolution and SNR are better discriminators between algorithms. The elemental Jacobian algorithm with a $\mathbf{R}_{diag}$ prior is the best all around reconstruction in terms of resolution. The nodal algorithm with the $\mathbf{R}_{diag}$ prior is competitive with its elemental counterpart in terms of both resolution and SNR. Conversion from nodal to

(a) $\mathbf{R}_{Tik}$ BR=.309, (b) $\mathbf{R}_{diag}$ BR=.233, (c) $\mathbf{R}_{HPF}$ BR=.279, SNR=.450   SNR=.337   SNR=.444
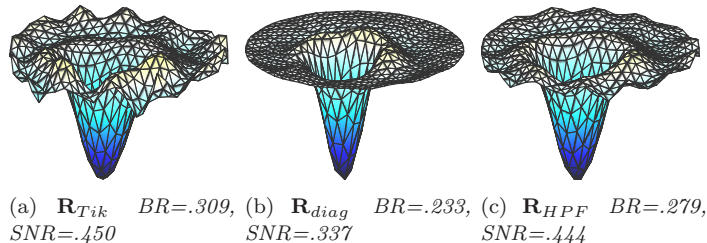
FIGURE 3. *Comparison of 2D Elemental reconstructions using tank data for different filters and Jacobians using 1024 element mesh. Reconstructions are normalized so that the vertical axis and color scales are maximized.*
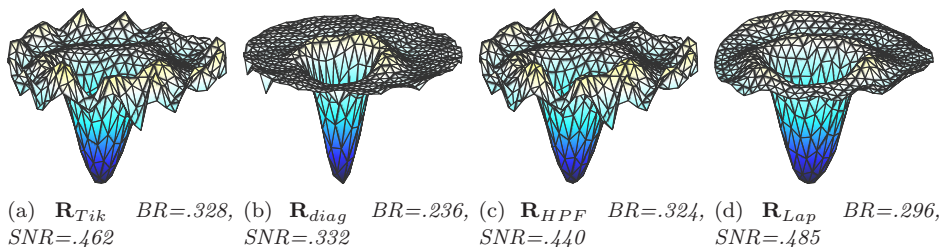

(a) $\mathbf{R}_{Tik}$ BR=.328, (b) $\mathbf{R}_{diag}$ BR=.236, (c) $\mathbf{R}_{HPF}$ BR=.324, (d) $\mathbf{R}_{Lap}$ BR=.296, SNR=.462   SNR=.332   SNR=.440   SNR=.485

FIGURE 4. *Comparison of 2D Nodal reconstructions using tank data for different filters and Jacobians using 1024 element mesh. Reconstructions are normalized so that the vertical axis and color scales are maximized.*

elemental basis, as described in section (2.4), imparts additional smoothing to the elemental solutions. This effect is not quantified here, however the elemental solutions do have the advantage of this additional smoothing. The solutions presented in figures 3 and 4 are in the elemental basis.

It is possible to improve the signal to noise ratio while maintaining the peak signal advantage of the nodal solutions by applying one or more stages of spatial filter discussed in 2.7. As shown in figure (5) the results are substantive. Repeated applications of the smoothing filter to the $\mathbf{R}_{diag}$ solution increase the SNR at the expense of peak amplitude and resolution. One or two passes of the filter can improve the SNR by 50% for a small cost in resolution.

The 2D results validate the applicability of the *Nodal Jacobian* algorithms by showing that for the configuration tested here, the nodal algorithm produces reconstructions as good as the elemental algorithms in terms of resolution and SNR. Moreover the nodal algorithms require less memory and run faster due to the smaller linear system that must be solved. Although not important for 2D reconstructions these speed and memory improvements allow the solution of larger systems inherent to 3D applications.

3.2. Hyperparameter Selection. The *BestRes* method of hyperparameter selection for 2D EIT is described in [7]. This method suggests selecting a hyperparameter that results in a reconstruction that has maximum resolution for an impulse contrast. The method was evaluated for 3D as follows. $\lambda_{BestRes}$ was evaluated
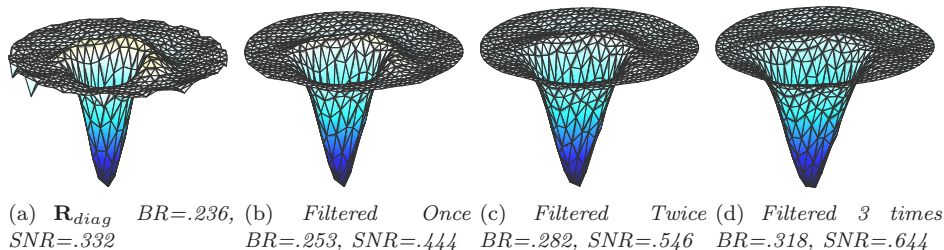
(a) $\mathbf{R}_{diag}$ $BR=.236$, SNR=.332 (b) *Filtered Once* $BR=.253$, $SNR=.444$ (c) *Filtered Twice* $BR=.282$, $SNR=.546$ (d) *Filtered 3 times* $BR=.318$, $SNR=.644$

FIGURE 5. *Spatial smoothing filter applied to nodal inverse solver algorithm with* $\mathbf{R}_{diag}$ *prior, 1024 element mesh. Reconstructions are normalized so that the vertical axis and color scales are maximized.*

as a function of radial position at the centre plane. For the $\mathbf{R}_{diag}$ prior the curve does not have a narrow minimum (is flat) for contrasts near the centre but becomes stable with a pronounced minimum for contrasts located between 20 and 75% of the radius from the centre. The curve becomes unstable for contrasts located at 85% radial position (close to the edge). The $\mathbf{R}_{Tik}$ curve remains flat for contrasts located near the centre and is unreliable until the contrasts are at radial positions between 30 and 65% to the edge. The resolution curve is very flat for the $\mathbf{R}_{Lap}$ prior but has detectable minimums that allow selection of the hyperparameter when the radial position of the target phantom is between 10% and 75%.

In [7] Graham and Adler recommend using $\lambda_{BestRes}$ calculated for a contrast located at r/2 for the 2D case. This suggestion is valid for the 3D case with the added rule that the contrast be located halfway between the electrode planes. Figure 6 shows resolution as a function of radial position and shows the effective ranges of the *BestRes* algorithm for a given priors.
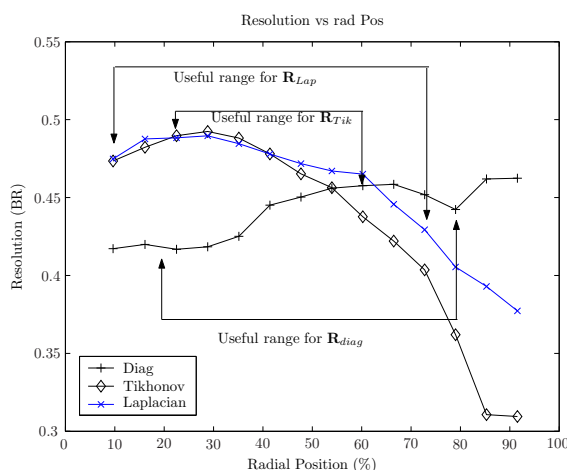

FIGURE 6. *Resolution vs Radial Position for* $\mathbf{R}_{Tik}$, $\mathbf{R}_{diag}$ *and* $\mathbf{R}_{Lap}$ *Priors*

3.3. 3D Simulation Results. Due to the excessive memory requirements it is not possible to calculate elemental solutions of the 3D models using 32 bit Matlab.

Consequently we do not evaluate the performance of the nodal 3D algorithm by comparison with its elemental counterpart. Rather we report on the performance of the nodal algorithms for 3D.

We calculated four sets of solutions, one for each prior, for each of the two data sets ($r = 0$ and $r/2$) described in section (2.8). These data sets were reconstructed using the FEM illustrated in figure (1(b)) and the hybrid adjacent protocol described in section (2.1).

Some reconstructions from the $r/2$ data set are shown in figure 7. This figure shows vertical slices through a one quarter section of the reconstructed tank for 3 different vertical positions of the impulse phantom. The leftmost column is the $\mathbf{R}_{Tik}$ prior, the centre column is the $\mathbf{R}_{diag}$, the right most is the $\mathbf{R}_{Lap}$ prior. We do not show the $\mathbf{R}_{HPF}$ solutions as they were similar to the $\mathbf{R}_{Tik}$ results.

From a qualitative point of view the three priors provide similar reconstructions in that none of them appears superior to the others in terms of a qualitative assessment of figure 7. Analysis of the various plots of figure 8 show that the $\mathbf{R}_{Tik}$ is inferior to the others in terms image energy while the $\mathbf{R}_{diag}$ prior is slightly superior in terms of resolution.

Figure 8(a) shows the resolution for all three priors for the two sets of simulated data, r=0 and r/2. The resolution varies by 20% as a function of height. The best resolution for each prior occurs near the electrode planes with the worse resolution occurring in the plane located halfway between the electrode planes. This is expected as resolution or its counterpart, sensitivity, decreases as position moves from current injecting or measuring electrodes. Thus resolution will be worse half way between the electrode planes. Radial position error as shown in figure 8(b) is lowest for contrasts at the centre of the tank and increases as contrasts move radially outward. In general however, the radial position error is small.

Height error as shown in figure 8(c) is common for all priors. There is a general tendency for contrasts to be reconstructed closer to the electrode planes than they actually are.

Position error is shown in figure 8(d) is a combination of the radial and vertical position errors and mainly indicates an asymmetry in the vertical axis. Figure 8(e) shows the variability of image energy as a function of target height. The $\mathbf{R}_{diag}$ and $\mathbf{R}_{Lap}$ priors provides the largest image energy but are also the most variable with respect to target vertical position. For example targets located in one of the electrode planes result in reconstructions with four times as much energy as the same target located at the extreme ends of the tank. Figure 8(f) shows the signal to noise ratio of the reconstructed images.

Overall the $\mathbf{R}_{diag}$ prior gives the best results however the difference between it and the $\mathbf{R}_{Lap}$ prior is minor. No work was completed for this paper concerning the effect of electrode plane separation on reconstruction performance.

3.4. Human Lung Data Results. The basic analysis of sections 3.1 and 3.3 are based on impulse contrasts which are not necessarily representative of complex contrasts. In order to test the *Nodal Jacobian Inverse Solver* for complex contrasts we reconstructed some lab data of human lungs using the $\mathbf{R}_{diag}$ prior. Data were measured from a human subject using the equipment and 3D protocol of section (2.1). The reconstruction shown in figure 9 was calculated in 12s on an AMD Athlon 64 3000+ with 2GB RAM using 45 iterations of Matlab's built-in preconditioned conjugate gradient function. The image on the left of figure 9 shows vertical planes of the 3D volume. The images on the right of figure 9 are two horizontal slices of the 3D reconstruction model. The lungs are readily observed in the two horizontal
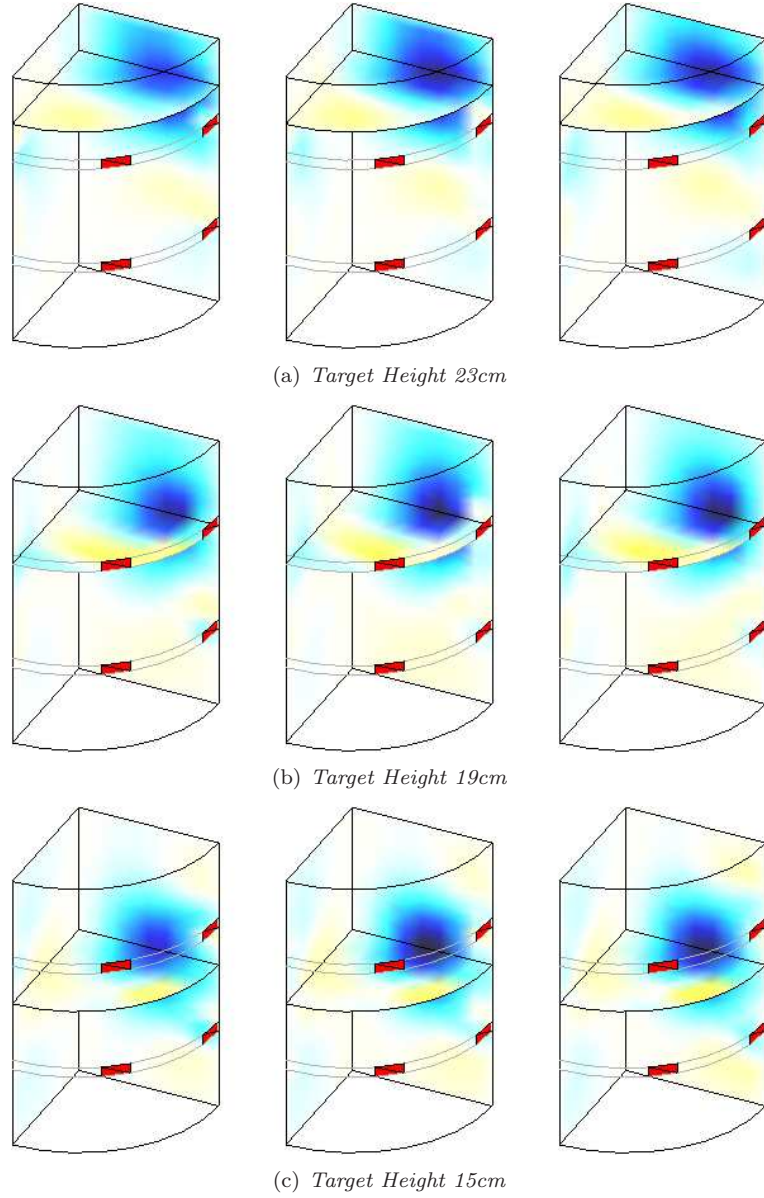
(a) *Target Height 23cm*

(b) *Target Height 19cm*

(c) *Target Height 15cm*

FIGURE 7. *Quarter section reconstructions of contrasts located at radial offset of r/2. Left column is* $\mathbf{R}_{Tik}$ *prior, centre column is* $\mathbf{R}_{diag}$ *prior, right column is* $\mathbf{R}_{Lap}$ *prior. Two electrodes per layer are shown*

slices. The vertical slice on the left shows that the vertical extent of the lungs does not extend to the vertical extremes of the 3D modeled volume. These results suggest that the *Nodal Jacobian* algorithm can be used for clinical applications.

(a) *Resolution*

(b) *Radial Position Error*

(c) *Height Error*
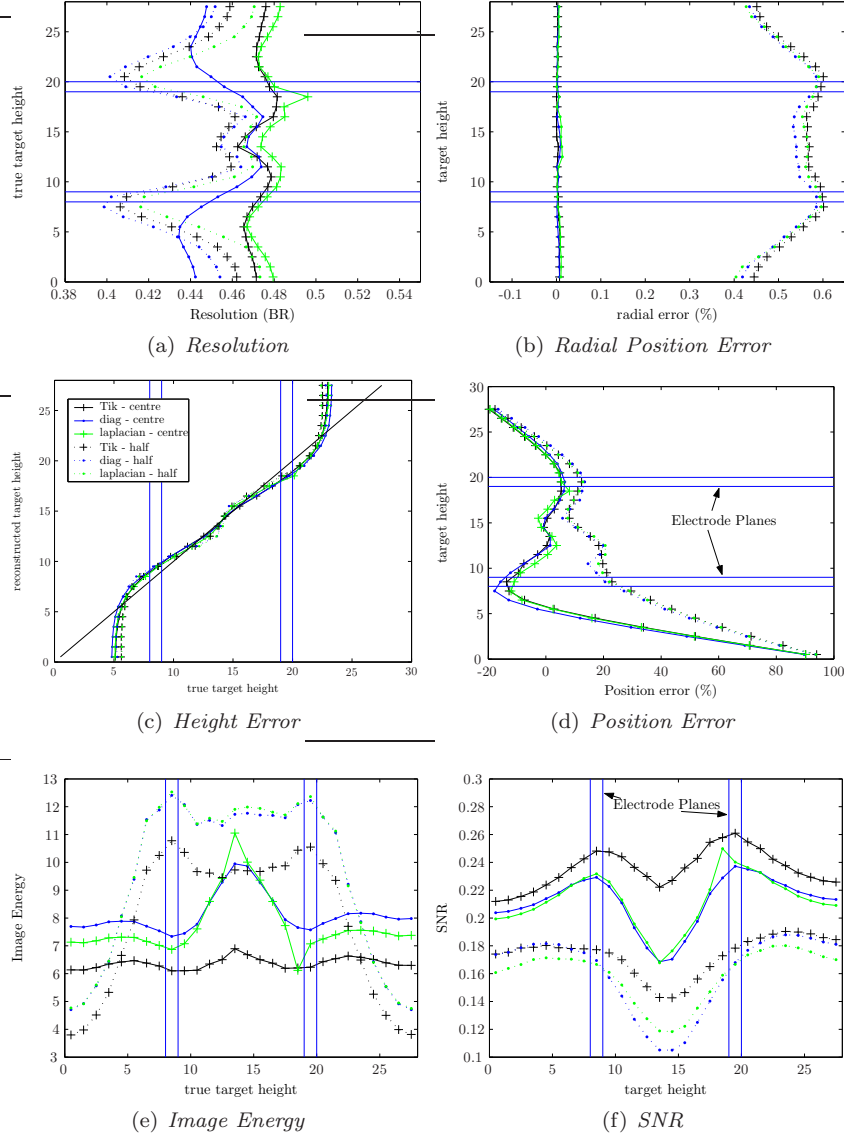
(d) *Position Error*

(e) *Image Energy*

(f) *SNR*

FIGURE 8. *Performance Measures for 3D Reconstructions of Two Simulated Data Sets. Legend in figure (c) applies to all figures. Electrode Planes are centered at heights of 8.5 and 19.5cm as indicated in 8(d) and 8(f)*

4. Discussion

This paper has presented a new family of algorithms for solving the inverse problem in EIT. The main advantage of the *Nodal Jacobian* algorithm is that it reduces the size of the linear system that must be solved. This allows the reconstruction of images from 3D models that are difficult or impossible to solve using element based algorithms. 16 electrode protocols were used in this work. Existing and future 3D EIT systems have 32, 64 or even 128 electrodes. The associated Jacobian will be
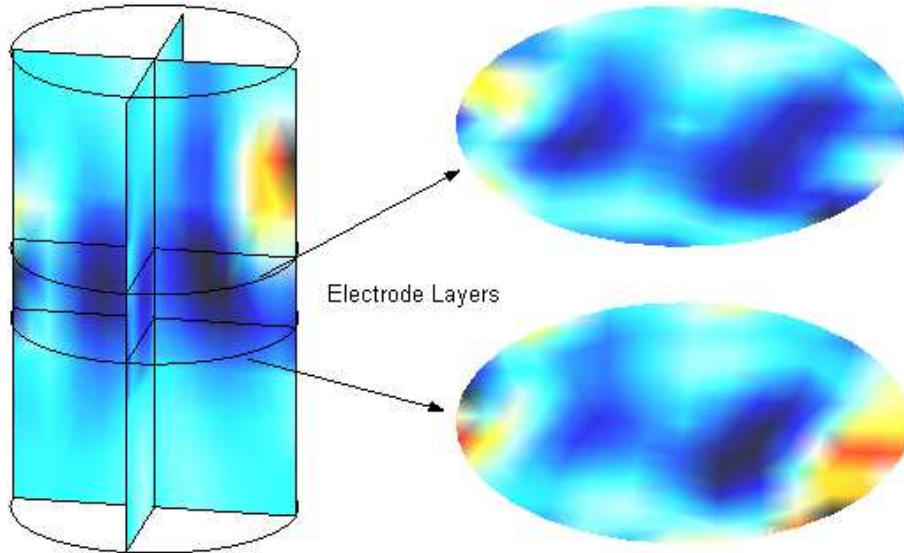
FIGURE 9. *Human Lung Data reconstructed using Nodal Jacobian Algorithm with the* $\mathbf{R}_{diag}$ *prior.*

large but it is possible to construct an elemental Jacobian for meshes with up to 130,000 elements with the 32 bit computers used in our lab. However the corresponding Hessian matrix will be too large to form, consequently such large models will be unsolvable using the elemental Jacobian via equation (6). The algorithm introduced in this paper reduces the computational requirements by a factor of up to 36 (26 for this paper's model) for dense 3D meshes and provides a promising way to solve high density 3D models with many electrodes. A secondary advantage of the nodal algorithm is the improvement in data extraction and rendering speeds which allow the display of multiple reconstructed image slices in real time.

The *Nodal Jacobian* algorithm is not an element or mesh free method, since the element based model is used to solve the forward problem and to calculate the elemental Jacobian from which the Nodal Jacobian is calculated. Future work could look at developing an algorithm to calculate a nodal Jacobian directly instead of calculating it from the elemental Jacobian.

Although the motivation for this work was to solve 3D problems, the *Nodal Jacobian Inverse Solver* algorithms produce solutions as good, in terms of resolution and SNR, as traditional algorithms for 2D configurations. 3D reconstructions from simulated data indicate that the *Nodal Jacobian Inverse Solver* with the $\mathbf{R}_{diag}$ or $\mathbf{R}_{Lap}$ prior is useful for imagining situations that have to date used an element based Jacobian with a smoothing prior. Finally, the successful reconstruction of a conductivity change image of human lungs from clinical data shows that the *Nodal Jacobian Inverse Solver* algorithm has good potential for clinical use.

References

[1] Adler, A. and Guardo, R., Electrical impedance tomography: regularised imaging and contrast detection, IEEE Trans. Med. Imaging, 15, 170-9.
[2] Adler, A. and Lionheart WRB., Uses and abuses of EIDORS: An extensible software base for EIT, Physiol Meas, in press.
[3] Barber DC. and Brown BH., Errors in reconstruction of resistivity images using a linear reconstruction technique, Clin. Phys. Physiol. Meas., 9, 101-4,1988.

[4] Borsic A.,McLeod CN., and Lionheart WRB., Total Variation Regularisation in EIT Reconstruction, Proceedings of the 2nd World Congress on Industrial Process Tomography, Page 433, 2001

[5] Cheney M., Isaacson D., Newell JC., Simske S. and Goble JC., NOSER: an algorithm for solving the inverse conductivity problem, Int. J. Imaging Syst. Technol, 2, 66-75, 1991.

[6] Gonzalez, Woods, Digital Image Processing Second Edition, Prentice Hall, 2002.

[7] Graham BM. and Adler A., Objective Selection of Hyperparameter for EIT, Physio. Meas., 27, 2006.

[8] Graham BM. and Adler A., Electrode Placement Strategies for 3D EIT, in press

[9] Kaipo JP, Kolehmainen V, Vauhkonene M, Somersalso E, Inverse problems with structural prior information, Inverse Problems 15:713:729, 1999.

[10] Lionheart WB.,EIT reconstruction algorithms: pitfalls, challenges and recent developments, Physiol. Meas., 25, 125-42, 2004 .

[11] Metherall P., Barber DC., Smallwood RH. and Brown BH.,Three dimensional electrical impedance tomography, Nature, 380, 509-12, 1996 .

[12] Polydorides N, Lionheart WRB.,A MATLAB based toolkit for three-dimensional Electrical Impedance Tomography: A contribution to the EIDORS project, Measurement Science and Technology, IoP Publishing, vol. 13, no. 12, pp. 1871-1883, December 2002.

[13] Polydorides N,. Image reconstruction algorithms for soft-field tomography, Ph.D. diss., UMIST, Manchester, UK, 2002.

[14] Vauhkonen M, Vadaósz D, Karjalainen PA, Somersalo E, and Kaipio JP, Tikhonov regularization and prior information in electrical impedance tomography, IEEE Trans Med Imaging, vol. 17, pp. 285-293, 1998.

[15] Vauhkonen M, Lionheart WRB, Heikkinen LM, Vauhkonen PJ, Kaipio JP: A MATLAB package for the EIDORS project to reconstruct two-dimensional EIT images. Physiol Meas 2001, 22:107-111.

[16] Vavasis SA, Stable finite elements for problems with wild coefficients. SIAM J. Numer. Anal., 33:890-916, 1996.

[17] Wheeler J, Wang W and Tang M.,A comparison of methods for measurement of spatial resolution in two dimensional circular EIT images, Physiol. Meas., 23, 169-76, 2002

[18] Yorkey TJ, Webster JG, Tompkins WJ, Comparing reconstruction algorithms for electrical impedance tomography, IEEE Trans. Biomed. Eng., vol. 34, pp. 843-852, 1987

School of Information Technology and Engineering (SITE), University of Ottawa, Canada
E-mail: graham.bm@sympatico.ca and adler@site.uottawa.ca
URL: http://www.site.uottawa.ca/ ∼adler/